





Research Article

Workspace analysis of 3-DOF U-shape base planar parallel robotic motion stage using shape memory alloy restoration technique (SMART) linear actuators

Deep Singh¹  · Rutupurna Choudhury² · Yogesh Singh² · Manidipto Mukherjee³

Received: 19 September 2020 / Accepted: 9 March 2021 / Published online: 29 March 2021

© The Author(s) 2021 

Abstract

The applications of lightweight planar parallel robotic manipulators are increasing enormously because of its various desirable characteristics such as low weight, lower inertia and higher stiffness. Higher accelerations and accuracies can be achieved in planar parallel manipulators. Also, shape memory alloy restoration technique (SMART)-based linear actuators are replacing huge and bulky linear actuators. This study presents the kinematic design of smart linearly actuated family of U-shape base planar parallel robotic manipulator. With the aid of solid modelling software, different available configurations were modelled and their workspace was analysed. The developed 3-DOF motion stages (18 unique configurations) were fabricated using fused deposition modelling process, and the top three configurations having higher workspace were further experimented. It is interesting to observe that the actual or experimental workspace of a particular manipulator configuration is further minimised from the predicted or feasible workspace. It is due to the presence of passive links, singularities, friction between the parts, heat dissipation, force distribution, stiffness, etc. The present study depicts the experimental workspace of the top three configurations, namely \underline{P} PR- \underline{P} RP- \underline{P} RR, \underline{P} RP- \underline{P} PR- \underline{P} RP and \underline{P} RP- \underline{P} PR- \underline{P} RR. Since none of the experimental workspace observed is equal or higher than the model workspace, an efficiency loss in terms of workspace reduction was calculated to understand the acceptability of the configurations in different domains. Apart from the loss, the result disclosed that the actual workspace of all the manipulators was within the feasible workspace domain of mobile platform. The \underline{P} PR- \underline{P} RP- \underline{P} RR manipulator was found to possess highest experimental workspace than other configurations. Note: \underline{P} , P, and R refer to active prismatic, passive prismatic and passive revolute joints respectively.

Keywords Nitinol · Micro-positioning · Planar parallel manipulators (PPMs) · Shape memory alloys

1 Introduction

Currently, robotics has gained numerous applications in almost every field. The need to automate various tasks in different robotic applications triggers the need for research. Numerous researches have been conducted based on applications and still seem to be an endless

research field, as it gains enormous importance. Till date, distinct robotic manipulators have been studied and still, numerous kinds are being proposed and studied in order to automate and thus reduce human effort. The notion of parallel manipulators is well recognized and well developed [1–3]. Today, parallel manipulators have a wide variety of applications covering fields such as medical,

Supplementary Information The online version contains supplementary material available at <https://doi.org/10.1007/s42452-021-04490-y>.

✉ Deep Singh, deepsingh_dh@srmuniv.edu.in | ¹Department of Mechanical Engineering, SRM Institute of Science and Technology, Chennai, Tamil Nadu, India. ²Department of Mechanical Engineering, National Institute of Technology Silchar, Silchar, Assam, India. ³Advanced Manufacturing Centre, CSIR-Central Mechanical Engineering Research Institute, Durgapur, West Bengal, India.



SN Applied Sciences (2021) 3:511 | <https://doi.org/10.1007/s42452-021-04490-y>

automotive, aerospace, military and space sectors. Parallel manipulators are greatly being applied for various other purposes such as cutting, welding, material handling, grinding, ship building, inspection, oil-well firefighting, ship-to-ship cargo handling, bridge construction, aircraft maintenance and steel erection [4].

Singh et al. proposed a five degrees of freedom based robotic manipulator which serves as goalkeeper in order to train football players [5]. The kinematic and dynamic study was carried out along with the torque analysis. Stewart platform, the well-known six-degree-of-freedom (DOF) spatial manipulator, has few limitations including a small and complex workspace, restriction of orientation angle and complex kinematics and dynamics system [6]. For these reasons, researchers begin to pay their attention to use lower-degree-of-freedom-based parallel manipulators, namely planar parallel manipulator (PPM). Parallel manipulators are also known as closed-loop manipulators [4]. The movement of PPM is restricted to a plane using prismatic and revolute joints [1–3, 7–39].

Despite being more workspace and dexterous manoeuvrability in serial robotic manipulators, PPMs gain more popularity and usage in real applications. This is because of the cantilever structure of the serial manipulators which leads to bending and also produces vibration at high speed which degrades the precision of the manipulators [4]. Parallel manipulators can take up more load as the entire load is shared by the parallel members and also provides more rigidity and stiffness with lesser inertia [4]. Also, the parallel manipulators undergo only compressive or tensile loads and no shear forces, bending and torsion moments [4]. Because of lower inertia, the parallel manipulators are also used for the purpose of flight simulators and fast pick-and-place robots [4, 40]. Parallel manipulators are more accurate as the errors are averaged as compared to serial robots in which errors are summed. It is because of the closed-loop architecture of the parallel links [4]. Despite parallel manipulators resulting in multiple inverse kinematic and direct kinematic solutions, it also provides more flexibility for the purpose of trajectory planning [41].

PPM consists of at least three limbs (kinematic chains) forming a mobile platform which is coupled to a fixed base by means of at least three limbs comprised of prismatic/revolute joint [7–39, 42]. These planar parallel motion stages have numerous applications, including material micro-machining, processing, material handling, fabrication, telescoping positioning systems and many more because of more straightforward joint arrangements [42]. In the past, many configurations such as 3-RRR, 3-PRR, 3-PPR, 3-PRP, 3-RRP, 3-RPP and 3-RPR and combinations of different limb configurations such as PRP + PPR + RRR have been proposed. Each configuration has its advantages and

limitations [1, 7–39]. Most of the designs for planar parallel manipulators are based on symmetric topology as it enhances the structural stiffness along with the manufacturing and assembly simplicity.

The kinematic analysis of three-degree-of-freedom 3-RRR planar parallel robotic manipulator has been studied by Chablat et al. with symmetric properties. Parallel manipulators exist with multiple direct kinematic solutions [41]. Since the stiffness of parallel manipulators plays an important role in deciding the positioning and orientation accuracies, Guanglei et al. [43] introduced a numerical method to decouple the Cartesian stiffness matrix into two and analysed it differently using eigenvalue problem to determine the manipulator stiffness for the 3-PPR PPM. The manipulator was studied under the influence of nonlinear actuation compliance [43]. Bai and Caro et al. proposed a 3-PPR PPM with an unsymmetrical base to maximize the robot's workspace. The manipulator results in amazing facts of decoupled degrees of freedom and large orientable workspace [44]. Gosselin and Angeles studied the kinematics of 3-RRR parallel manipulators to maximize the workspace [45].

The equilateral triangular base-based symmetric planar parallel robotic manipulator provides higher structural stiffness but may not deliver larger workspace, compactness, modularity and simple structure. To overcome the limitations, a new family of 3-DOF planar parallel manipulator was proposed. The proposed family of PPM is comprised of three limbs mounted on the base of a square or 'U' shape. The first joint of each limb is the active prismatic joint, and the SMART actuator was used for bidirectional linear actuation [46].

AbuZaiter et al. [47] have developed a miniaturized Stewart platform which actuates using TiNiCu-based SMA actuators. It provides translational motion along z-axis along with tilting motion using 4 SMA springs. AbuZaiter et al. [48] also developed a SMA-actuated micro-positioning stage using six SMA springs. The developed stage possesses 3-DOF to move smaller objects for microscopic scanning applications. Sreekumar et al. [49] presented the development of a compliant parallel manipulator actuated by SMA wire. The experiment resulted large deflection analysis, and the device is suitable for various applications in space, medical, etc. Santhakumar et al. [50] studied the forward and inverse kinematics along with the workspace of three-legged U-shape base 3PRP planar robotic manipulator experimentally by implementing nitinol spring, a shape memory alloy (SMA), as an actuator. The nitinol serves as a linear actuator and actuates on the supply of electrical current across it. The end-effector pose and the workspace of the manipulator were analysed in the absence of a feedback loop (open-loop condition). Deep

et al. [51] have also presented the experimental workspace associated with the U-shape base 3PRP, PPR-2PRP and PRR-PRP PPMs incorporating SMART actuator. Although the performance of few of the PPMs is evaluated, there is a need to identify the significance of each of the eighteen U-shape base PPMs as discussed in Sect. 2. The workspace, singularity and kinematic isotropy associated with each of the discussed PPMs vary due to the variation in the design of each limb. Hence, identification of workspace associated with the manipulators can highly influence its application in a wide domain of micro-manufacturing, micro-fabrication, etc.

In the present study, the workspace associated with the family of U-shape 3-DOF PPM is analysed by the smart actuation technique of the active input translational joints. The smart actuation refers to the implementation of SMA-based smart material actuator, here referred to as a SMART (shape memory alloy restoration technique) linear actuator. Each of the eighteen U-shape base PPMs is evaluated for the associated workspace, and each of the manipulators can be implemented for a variety of applications based on its work region.

1.1 Shape memory alloy restoration technique (SMART) linear actuator

SMA is one of the most wonderful materials because of its ability to memorize shapes due to thermally induced solid-state phase transition. The composition of SMA helps in providing different mechanical characteristics such as ductility, corrosion and also memory [52]. SMA is very unique material that changes its shape, position, stiffness, natural frequency and various other mechanical properties with the variation in temperature. Because of such unique mechanical behaviour, SMA is hugely studied [53, 54].

SMA has gained much importance in the application as actuators because of its high energy density, clean and silent actuation. The phase transformation in an SMA takes place between a low crystallographic symmetry (monoclinic crystal structure) martensitic phase to a high symmetry (cubic crystal structure) austenitic phase under thermal loading. At low temperatures and high stresses, the martensite shows stability, and at high temperatures and low stresses, the austenite shows stability [51, 52]. Some of the SMA is Cu–Zn, Cu–Al–Ni, Ni–Ti, Ni–Ti–Fe, Cu–Zn–Al, Fe–Pt and many more.

Nitinol (NiTi), a shape memory alloy, exhibits the characteristics shape memory effect (SME) and super-elasticity depending on the working temperature. The composition of nitinol is 50% nickel and 50% titanium. The maximum recoverable strain is fixed for a fix SMA. However, applying

higher stress also induces more elastic strain [55]. Nitinol is comparatively better than the CuZnAl and CuAlNi based on multiple thermo-mechanical performances, including biocompatibility [54, 56]. SMA actuators are gaining huge popularity as they are very compact with higher power/mass ratio and low voltage activation [54]. One of the main characteristics of SMA is hysteresis which makes complications in controlling the displacement because of its continuous nonlinear variation in length. The difference between the forward and reverse transformation paths results in hysteresis [57].

The SMA-based actuators can be operated by the Joule heating process. On supply of direct current (DC) across the SMA, the temperature of the actuator rises due to the presence of electrical resistance of the SMA-based wire and springs. Due to the increase in temperature, the SMA-based actuators (at the pre-stretched condition) undergo a phase transformation from martensite to austenite resulting in contraction (or torsion, in case of spring-based SMA) of the SMA. The rate of contraction increases with the rise in value of the current and vice versa. Singh et al. have also categorized the current into four based on the actuation and precision attained by the Nitinol SMA spring, as depicted in Fig. 1 [53]. ' V_c ' represents the rate of contraction of the spring (or rate at which the overall length of the spring decreases) against each category, for a change in length (or retraction) of 71 mm (pre-stretched initial length = 100 mm, final length = 29 mm). Recently, SMA is being used in various fields such as biomedical, commercial and aerospace industries. DesRoches et al. [58] studied the potential of Ni–Ti SMA for application in seismic-resistant design and retrofit. Khidir et al. [59] presented a technique and its feasibility to actuate PPMs using SMA-based linear actuators.

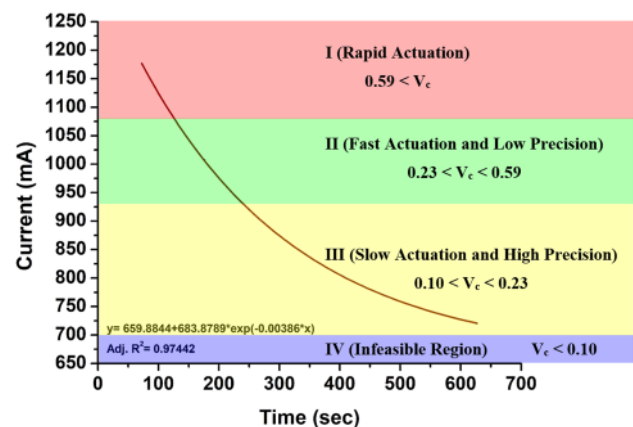


Fig. 1 Exponential plot of current vs. time for contraction of pre-stretched nitinol spring [53]

2 Family of U-shape base planar parallel manipulators

The family of U-shape base PPMs possesses three legs (limbs) of which one is oriented along the X-axis and the other two oriented along the Y-axis, forming the fixed base of the shape 'U'. In this respect, it is possible to develop a PPM with three limbs using eight serial (open-loop) limbs, namely PPP, PPR, PRP, PRR, RRR, RPR, RRP and RPP. The first joint at each limb of the 3-DOF planar parallel manipulator is considered to be an active prismatic joint (P) because of its multiple advantages such as modular design, back drivability, compactness, reduction in the link interferences, large singularity-free

workspace, simple kinematic arrangement, ease of control and low inertial properties of the moving system [1–3, 16, 60]. Hence, out of the above-mentioned eight kinematic limbs, only four limbs could develop a U-shape base 3-DOF PPM, namely PPP, PPR, PRP and PRR. Out of these four limbs, PPP limb is avoided to develop 3-DOF PPM as it does not allow rotation to the mobile platform (end-effector) of the manipulator. Therefore, only three limbs, namely PRP, PPR and PRR, are feasible for implementation in the manipulator. Thus, based on repetition theory of permutation and combination, three limbs (PRP, PPR and PRR) are implemented to develop 3-DOF PPM which leads to $3^3 = 27$ manipulators as represented in Fig. 2. However, it can be clearly seen that 9 out of

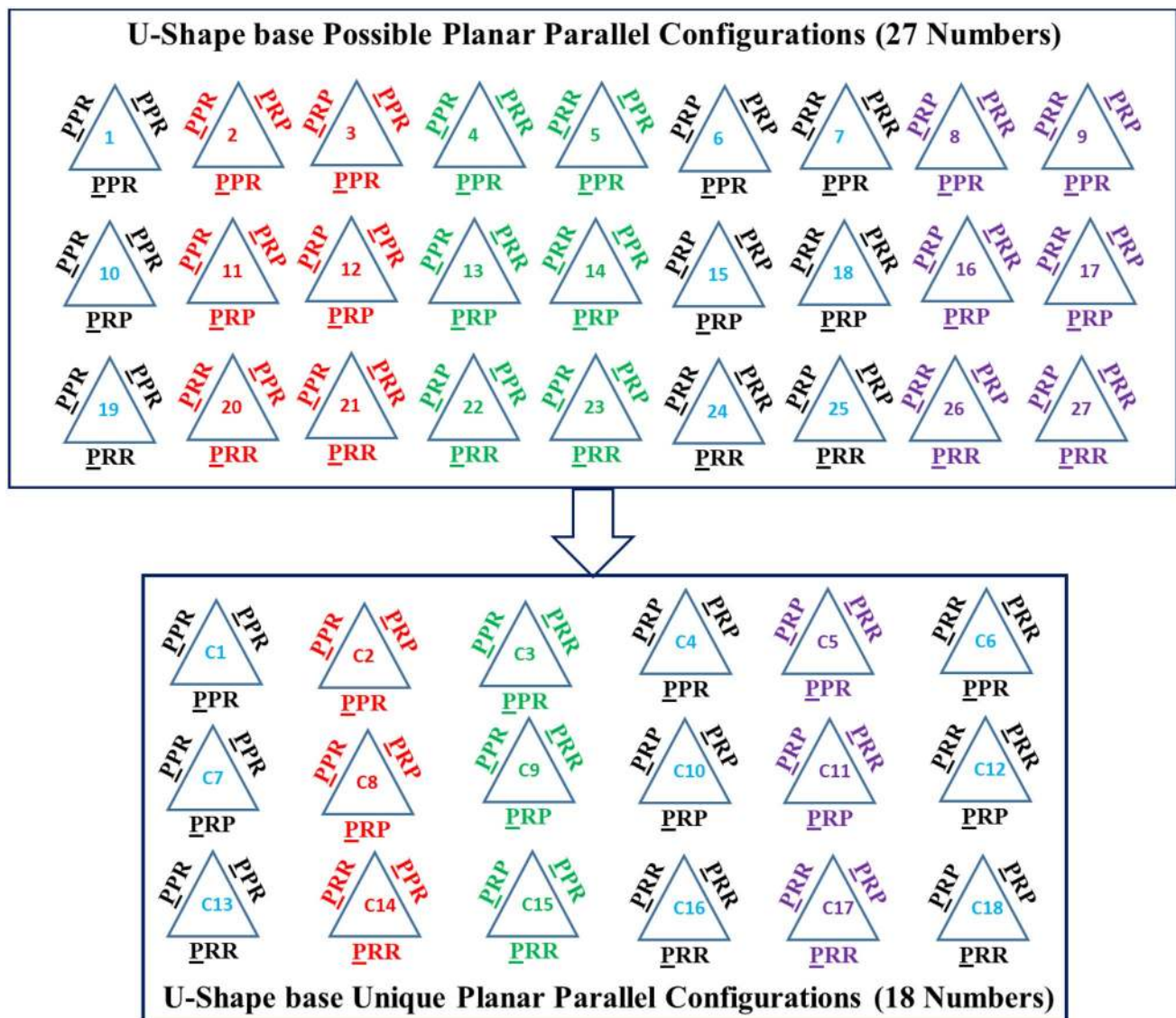


Fig. 2 Family of U-shape base planar parallel manipulator

27 manipulators are repeated which results in 18 unique and non-repetitive manipulators as illustrated in Fig. 2 [51]. The nomenclature of the manipulators has been presented uniquely, as represented in Fig. 2. The letter 'C' stands for 'Configuration' followed by the manipulator number such as C1, C2, C3 and so on. This nomenclature is short and helps in easy referencing in the paper. Each manipulator in the proposed 'U' shape family possesses 3-DOF with the configuration of the end-effector given as (x, y, θ_z) .

These manipulators will, however, be applied in the implementation of different applications depending on the workspace associated with each manipulator. Therefore, it is important to define the workspace for each manipulator. This study introduces the workspace analysis correlated with each manipulator. Every limb of this family of manipulator begins with an active prismatic joint followed by passive joints and links which connects fixed base to the end-effector.

A very effective tool for determining the workspace is the kinematics of a parallel manipulator. In addition, it is very difficult to design and control the manipulator without the kinematic solution or the workspace [42].

3 Geometrical and kinematic arrangements of the family of U-shape base manipulators

The frame arrangement of the fixed and mobile platform is denoted by 'O' and 'Q', respectively. These frames play a crucial role in describing the kinematic solution of the manipulator through the associated link and joint parameters.

The shape of the end-effector considered is an equilateral triangle of side length 'a' and height 'h' connected to the fixed U-shape base platform by three limbs. Active joint displacement is denoted by ' r_i ' ($i=1,2,3$). The link length of the connecting members connecting the active prismatic joint and the end-effector is denoted by ' l_j ' ($j=1,2,3$). 's' and 'h' are the width and height of the fixed U-shape base, respectively. The orientation (rotation about the z-axis) of the mobile platform is denoted by ' θ_z ', and the design angles of the configurations are denoted by ' θ_k '. ($k=1,2,3,4$).

Figure 3 depicts the kinematic configurations of limbs PPR, PRP and PRR. Figure 3 also provides the correlation between the active translational joint and the pose of the end-effector under various conditions like the same or different limbs associated with the development of a 3-DOF PPM. All the active controllable inputs are considered as active prismatic (translational) inputs for the design and analysis.

Jacobian matrix (J) of any configuration (18 manipulators) refers to the velocity transformation/mapping matrix which maps the Cartesian space velocities to the joint space velocities. The Jacobian matrix for the U-shape fixed-base manipulators is mentioned in Table 1. Jacobian matrix dictates the singularity associated with any manipulator within the given workspace region. The singular positions represent $\|J\|=0$ [36, 46]. Kinematic isotropy also dictates the overall performance of the manipulators. The higher the kinematic isotropy, the larger is the associated workspace and vice versa. Mohanta et al. [46] have presented the kinematic isotropies of all the 18 PPMs and their effect on the associated overall workspace performance. Singh et al. [M] have also presented the overall workspace associated with the PPMs with varying shape of the fixed base.

4 U-shape base 3-DOF planar parallel manipulator with SMART linear actuator

The family of U-shape base PPMs varies in configuration based on the location of active prismatic, passive prismatic and passive revolute joints. Each manipulator has three limbs—one along X-axis and the other two along the Y-axis. The limb along X-axis is referred to as limb-1, the left limb along Y-axis is referred as limb-2, and the right limb along Y-axis is referred as limb-3. Each limb consists of two nitinol (NiTi) springs for bidirectional actuation and serves as an active prismatic joint or the joint space displacement (r_1, r_2 and r_3). As discussed, eighteen unique manipulators can be developed by configuring the limbs with PPR, PRP and PRR.

To explain it in a better way, the manipulator C9 with its three limbs is depicted in Fig. 4. Here, the combination of limb used is PRP + PPR + PRR. The limb-1 of this manipulator is configured as PRP in which the first P represents the active translational joint actuated by SMA spring and also it has the ability to rotate passively at the joint (7) as shown in Fig. 4. Another link connected with the end-effector and passing through joint (7) serves as a passive translational or prismatic joint.

The limb-2 of this manipulator is configured as PPR, in which the first P represents an active translational joint (8). Another link also translates about the point (8) along X-axis which further connects with the end-effector with the passive revolute joint.

The limb-3 of this manipulator has been configured as PRR in which the first P represents active translational joint (9) similar to leg-1 and leg-2 actuated by SMA springs. Another link is connected to the active translational joint at (9) by the passive revolute joint on one end. The other end is connected to the end-effector with the help of another passive revolute joint. Similarly, all the eighteen

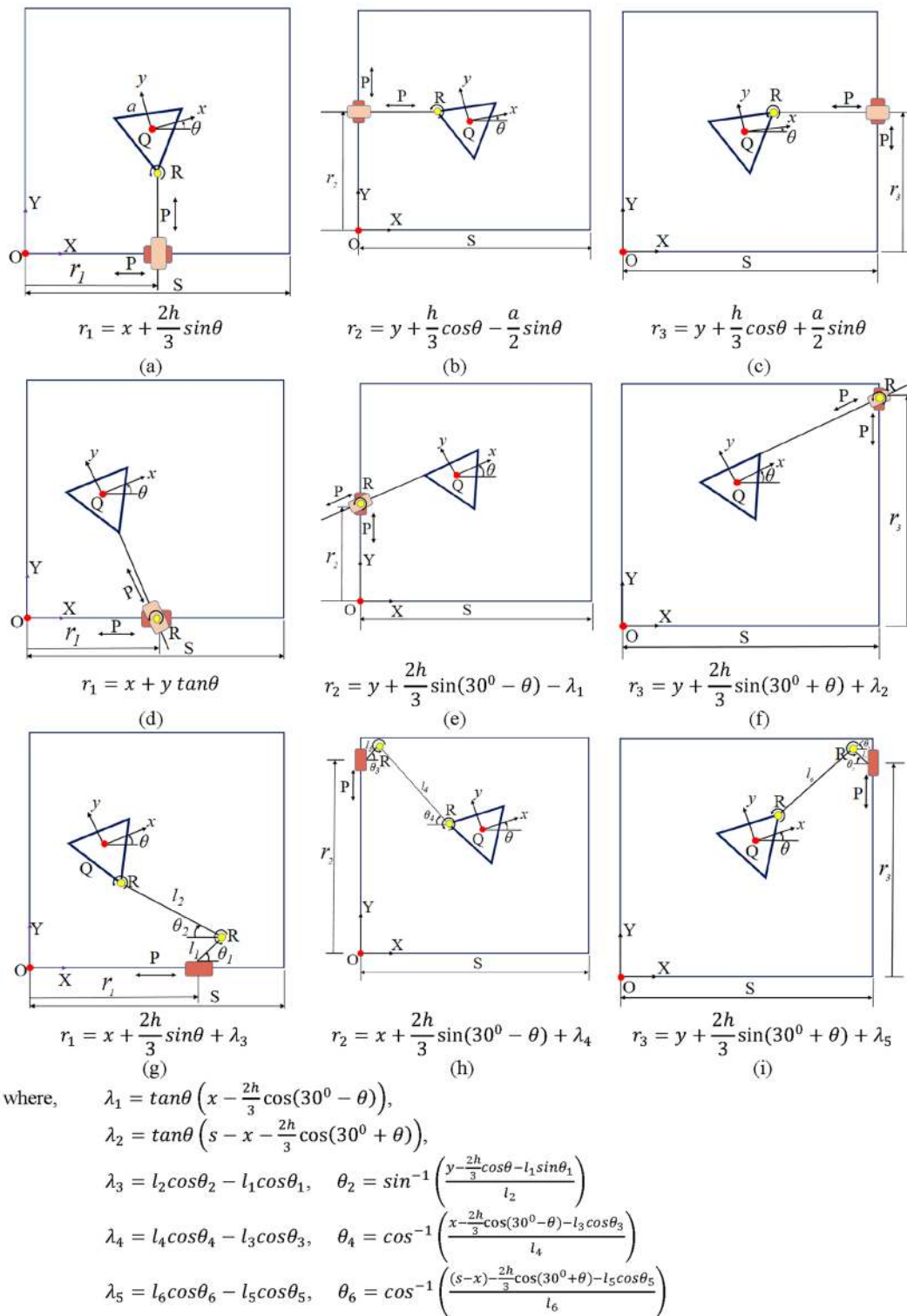


Fig. 3 Frame diagrams of the family of U-shape fixed-base planar parallel manipulators

manipulators can be obtained by assembling the three limbs with PPR or PPR or PRR. The presence of two nitinol SMA springs at each of the limbs (if implemented as shown

in Fig. 4) leads to bidirectional translational motion along its axis.

The regulated DC current is supplied to only one spring in the first P joint (developed using SMA spring) of each

Table 1 Jacobian matrix (J) of the family of U-shape fixed-base planar parallel manipulators

$\begin{bmatrix} 1 & 0 & \frac{2h}{3} \cos \theta \\ 0 & 1 & \lambda_{15} \\ 0 & 1 & \lambda_{14} \end{bmatrix}$	$\begin{bmatrix} 1 & 0 & \frac{2h}{3} \cos \theta \\ 0 & 1 & \lambda_{15} \\ -\tan \theta & 1 & \lambda_8 \end{bmatrix}$	$\begin{bmatrix} 1 & 0 & \frac{2h}{3} \cos \theta \\ 0 & 1 & \lambda_{15} \\ \lambda_9 & 1 & \lambda_6 - \lambda_7 \lambda_9 \end{bmatrix}$
(a) Configuration 1 (C1)	(b) Configuration 2 (C2)	(c) Configuration 3 (C3)
$\begin{bmatrix} 1 & 0 & \frac{2h}{3} \cos \theta \\ -\tan \theta & 1 & \lambda_{12} \\ -\tan \theta & 1 & \lambda_8 \end{bmatrix}$	$\begin{bmatrix} 1 & 0 & \frac{2h}{3} \cos \theta \\ -\tan \theta & 1 & \lambda_{12} \\ \lambda_9 & 1 & \lambda_6 - \lambda_7 \lambda_9 \end{bmatrix}$	$\begin{bmatrix} 1 & 0 & \frac{2h}{3} \cos \theta \\ -\lambda_{13} & 1 & -\lambda_{10} - \lambda_{11} \lambda_{13} \\ \lambda_9 & 1 & \lambda_6 - \lambda_7 \lambda_9 \end{bmatrix}$
(d) Configuration 4 (C4)	(e) Configuration 5 (C5)	(f) Configuration 6 (C6)
$\begin{bmatrix} 1 & \tan \theta & y \sec^2 \theta \\ 0 & 1 & \lambda_{15} \\ 0 & 1 & \lambda_{14} \end{bmatrix}$	$\begin{bmatrix} 1 & \tan \theta & y \sec^2 \theta \\ 0 & 1 & \lambda_{15} \\ -\tan \theta & 1 & \lambda_8 \end{bmatrix}$	$\begin{bmatrix} 1 & \tan \theta & y \sec^2 \theta \\ 0 & 1 & \lambda_{15} \\ \lambda_9 & 1 & \lambda_6 - \lambda_7 \lambda_9 \end{bmatrix}$
(g) Configuration 7 (C7)	(h) Configuration 8 (C8)	(i) Configuration 9 (C9)
$\begin{bmatrix} 1 & \tan \theta & y \sec^2 \theta \\ -\tan \theta & 1 & \lambda_{12} \\ -\tan \theta & 1 & \lambda_8 \end{bmatrix}$	$\begin{bmatrix} 1 & \tan \theta & y \sec^2 \theta \\ -\tan \theta & 1 & \lambda_{12} \\ \lambda_9 & 1 & \lambda_6 - \lambda_7 \lambda_9 \end{bmatrix}$	$\begin{bmatrix} 1 & \tan \theta & y \sec^2 \theta \\ -\lambda_{13} & 1 & -\lambda_{10} - \lambda_{11} \lambda_{13} \\ \lambda_9 & 1 & \lambda_6 - \lambda_7 \lambda_9 \end{bmatrix}$
(j) Configuration 10 (C10)	(k) Configuration 11 (C11)	(l) Configuration 12 (C12)
$\begin{bmatrix} 1 & -\lambda_{14} & \lambda_{16} \\ 0 & 1 & \lambda_{15} \\ 0 & 1 & \lambda_{14} \end{bmatrix}$	$\begin{bmatrix} 1 & -\lambda_{14} & \lambda_{16} \\ 0 & 1 & \lambda_{15} \\ -\tan \theta & 1 & \lambda_8 \end{bmatrix}$	$\begin{bmatrix} 1 & -\lambda_{14} & \lambda_{16} \\ -\tan \theta & 1 & \lambda_{12} \\ -\tan \theta & 1 & \lambda_8 \end{bmatrix}$
(m) Configuration 13 (C13)	(n) Configuration 14 (C14)	(o) Configuration 15 (C15)
$\begin{bmatrix} 1 & -\lambda_{14} & \lambda_{16} \\ -\lambda_{13} & 1 & -\lambda_{10} - \lambda_{11} \lambda_{13} \\ 0 & 1 & \lambda_{14} \end{bmatrix}$	$\begin{bmatrix} 1 & -\lambda_{14} & \lambda_{16} \\ -\lambda_{13} & 1 & -\lambda_{10} - \lambda_{11} \lambda_{13} \\ -\tan \theta & 1 & \lambda_8 \end{bmatrix}$	$\begin{bmatrix} 1 & -\lambda_{14} & \lambda_{16} \\ -\lambda_{13} & 1 & -\lambda_{10} - \lambda_{11} \lambda_{13} \\ \lambda_9 & 1 & -\lambda_6 - \lambda_7 \lambda_9 \end{bmatrix}$
(p) Configuration 16 (C16)	(q) Configuration 17 (C17)	(r) Configuration 18 (C18)

where

$$\begin{aligned} \lambda_6 &= \frac{2h}{3} \cos(30^\circ + \theta) & \lambda_7 &= \frac{2h}{3} \sin(30^\circ + \theta) \\ \lambda_8 &= \lambda_6 + \lambda_7 \tan \theta + \frac{\sec^2 \theta}{\tan \theta} \lambda_3 & \lambda_9 &= \frac{\sin \theta_6}{\sqrt{l_6^2 - \sin^2 \theta_6}} \\ \lambda_{10} &= \frac{2h}{3} \cos(30^\circ - \theta) & \lambda_{11} &= \frac{2h}{3} \sin(30^\circ - \theta) \\ \lambda_{12} &= -\lambda_{10} + \lambda_{11} \tan \theta - \frac{\sec^2 \theta}{\tan \theta} \lambda_2 & \lambda_{13} &= \frac{\sin \theta_4}{\sqrt{l_4^2 - \sin^2 \theta_4}} \\ \lambda_{14} &= -\frac{h}{3} \sin \theta + \frac{a}{2} \cos \theta & \lambda_{15} &= -\frac{h}{3} \sin \theta - \frac{a}{2} \cos \theta \\ \lambda_{16} &= \frac{2h}{3} \cos \theta - \lambda_{14} \frac{2h}{3} \sin \theta \end{aligned}$$

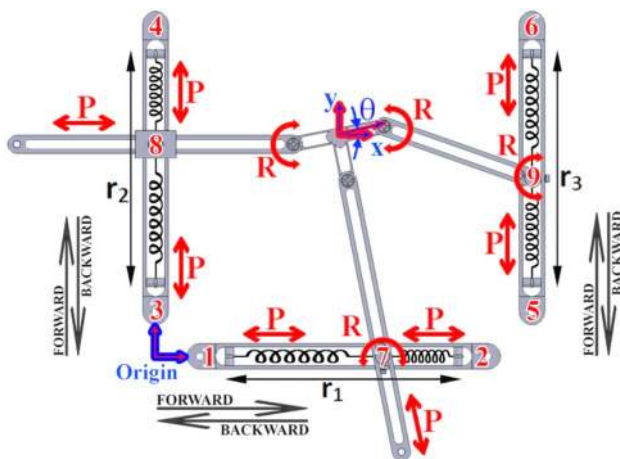


Fig. 4 PRP-PPR-PRR manipulator (C9)

limb, and the corresponding spring starts contracting which ceases after some time. This results in the elongation of the other spring connected in series in the same leg. Ultimately, the position of the connector (7, 8, 9 as shown in Fig. 4) of the two springs or active input translational joints as depicted in Fig. 4 varies. This, thereby, leads to variation in the pose of the end-effector.

5 Experimental procedure

5.1 Material selection and specification

The linear actuator considered for the active translation joint of the manipulator is a one-way nitinol SMA spring of 0.75 mm wire diameter with 19 helix windings. The NiTi SMA spring can contract maximum up to 29 mm when thermally induced under no external load. Under

Table 2 Properties of nitinol SMA [58]

Property	Value
Density	6.45 g/cm ³
Young's modulus	70 GPa
Poisson's ratio	0.33
Tensile yield strength	559 MPa
Compressive yield strength	560 MPa
Tensile ultimate strength	960 MPa
Compressive ultimate strength	960 MPa

Table 3 FDM process parameter values

Process parameters	Value
Raster width	0.016 mm
Raster angle	0°
Built material tool tip	T16
Support material tool tip	T12
Air gap	0 mm

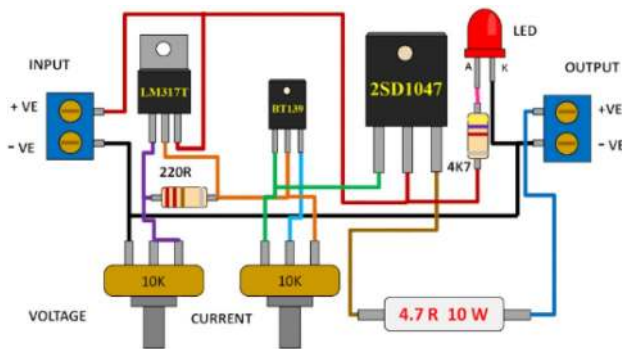


Fig. 5 Circuit diagram of variable DC power supply

external load, the spring can be elongated up to 140 mm. These SMA springs can also be used in series for longer distances and also in parallel for higher force capability. The various physical properties of nitinol are presented in Table 2 [58]. A single spring, under no load condition, activates instantly (< 1 s) for current, $I \geq 2$ A. For current under $700 \text{ mA} < I < 2$ A, the activation time for the nitinol spring ranges from 1 to 3 s. The springs when supplied a direct current of less than 700 mA requires larger activation time which is greater than 3 s.

5.2 DC power supply

In order to actuate the nitinol springs, there is a need to elevate its temperature to the austenite region of pre-stretched nitinol which leads to phase transformation. The temperature of the SMA springs is raised by passing current through it using a variable DC power supply. The circuit diagram for the developed variable DC power supply is depicted in Fig. 5. The minimum current deviation obtained by the prototype is 10 mA. Supply of electrical current through the nitinol spring increases its temperature due to its electrical resistance, also known as Joule heating, which results in phase transition and change in size of the pre-stretched nitinol spring.



Fig. 6 RPT 3D part models printed using Stratasys FDM 360mc

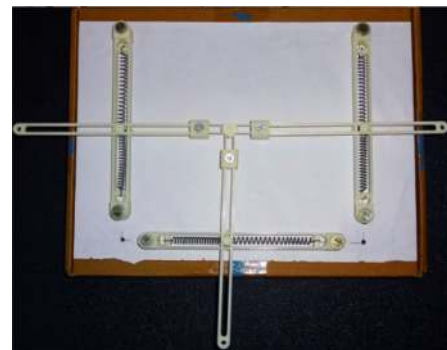


Fig. 7 Assembled C10 configured PPM

5.3 Development of the prototype

Rapid prototyping is employed for the rapid fabrication of 3D CAD part models by fused deposition modelling (FDM), an additive manufacturing technology. Acrylonitrile butadiene styrene-M30 (ABS), a thermoplastic material by Stratasys, is used as the part build material. The support material used is SR-30 water-soluble support by Stratasys. The various process parameters used in the FDM process for 3D printing of various parts are mentioned in Table 3.

The CAD model was printed using the Stratasys FDM 360mc machine, and the various 3D printed parts are depicted in Fig. 6. The components shown in Fig. 6 have been used to make the assembly of the C10 configured

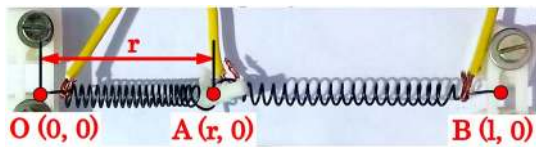


Fig. 8 Nitinol SMA springs arranged in series

PPM, as shown in Fig. 7. Also, other manipulators can be obtained by proper assembly of the parts.

5.4 Experimental model of a limb with two SMA springs

To evaluate the behaviour of SMA springs connected in series, a model, depicted in Fig. 8, has been developed to mitigate the design of a limb (or leg) of the manipulator. One end of first spring is fixed at the Origin (0, 0) and one end of the other spring is fixed at B(l,0), where l= 129 mm. The other ends of the springs are together at the point A(r, 0) with the help of a pin made of ABS plastic. In this configuration, when direct current is supplied to any of the

spring, the other spring reacts and opposes the retraction of the active SMA spring. Due to the presence of opposing force, the SMA stops retracting (under current supply), when it reaches a length of approximately 20 mm (under 1 mA < l < 2 mA). The activation response of the nitinol spring, under this configuration, ranges from 3 to 7 s for the direct current ranging from 1 to 2 mA. Initially, the right spring is contracted to get the desired position of A (at t=0 s). Once the position is reached, 1220 mA of direct current was supplied to the left spring for exactly 100 s and the retraced distance was measured as presented in Table 4. The same experiment was carried out for 5 different current values with 5 repetitions as presented in the table. The table dictates that the retraction length decreases with the decrease in current supply. Also, it is evident that the performance and repeatability of the SMA-based actuator is quite high.

5.5 Experimental Set-up for the Workspace Analysis

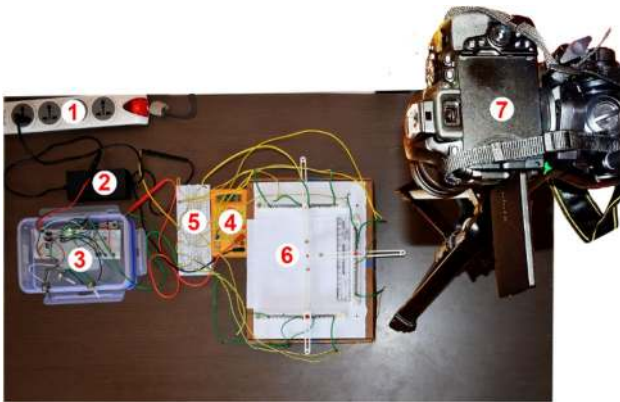
In order to perform the experiment to observe the workspace of the 3-DOF U-shape base PPMs using SMART

Table 4 Retraction length of SMA spring (in series) at varied direct current

Current (mA)	Initial length (mm)	Final length (mm)	Retraction length (mm)	Mean retraction length with standard deviation (mm)
1220	74.20	41.23	32.97	32.94 ± 0.027
	74.20	41.27	32.93	
	74.20	41.26	32.94	
	74.20	41.24	32.96	
	74.20	41.30	32.90	
1160	75.50	43.91	31.59	31.60 ± 0.018
	75.50	43.88	31.62	
	75.50	43.93	31.57	
	75.50	43.90	31.60	
	75.50	43.90	31.60	
1130	73.80	45.32	28.48	28.50 ± 0.024
	73.80	45.30	28.50	
	73.80	45.30	28.50	
	73.80	45.26	28.54	
	73.80	45.32	28.48	
1120	84.00	66.78	17.22	17.19 ± 0.019
	84.00	66.81	17.19	
	84.00	66.83	17.17	
	84.00	66.80	17.20	
	84.00	66.82	17.18	
1060	73.00	63.21	9.79	9.80 ± 0.012
	73.00	63.18	9.82	
	73.00	63.21	9.79	
	73.00	63.20	9.80	
	73.00	63.20	9.80	

Table 5 Experimental set-up units

Sl. No.	Experimental set-up units
1	Extension board
2	AC/DC adapter
3	Variable DC power supply
4	Multimeter
5	Breadboard
6	Planar parallel manipulator
7	Digital camera with tripod

**Fig. 9** Experimental set-up

linear actuators, an experimental set-up has been developed. The experimental set-up includes various units, as mentioned in Table 5. The set-up is also depicted in Fig. 9.

In the experimental set-up, the AC/DC adapter (2) receives AC from the extension board (1) and converted the DC serves as input to the variable DC power supply (3). The current is regulated with the help of a potentiometer attached to the variable DC power supply. The regulated DC is monitored using the multimeter (4). The current is then supplied to the SMART linear actuator of the PPM (6) through the breadboard. The breadboard (5) helps in directing the regulated current to the SMA springs in the manipulator limbs in various combinations. The Digital Camera (Nikon D5600) is mounted on a tripod (7) to track the pose of the end-effector of the manipulator.

6 Workspace analysis

6.1 Workspace analysis of CAD models

The assembled CAD models of all the 18 manipulators have been used to determine the associated workspace. As the experiment resulted in 29 mm of total contraction for a single spring under no external load condition, the same

has been incorporated in the CAD models. The maximum contraction of NiTi SMA springs associated at each of the three limbs has been made limited to 29 mm. The active prismatic joints are then allowed to translate on consideration of physical dynamics. The pose of the manipulator's end-effector is allowed to vary in various combinations of its input translational joints. The movement of active translational joint r_1 along positive X-axis direction is considered as forward movement (F) and along negative X-axis is considered as backward (B) movement. Similarly, the movement of active translational joints r_2 and r_3 along positive Y-axis direction is considered as forward movement (F) and along negative Y-axis is considered as backward (B) movement. Hence, seven different combinations of input translational joints have been considered for workspace analysis, as tabulated in Table 6. Again, these seven combinations have further been divided into various combinations based on the actuation direction (F or B) of the input translational joints. The workspace so obtained based on maximum NiTi SMA spring contraction (29 mm) is referred to be the "Ideal Workspace" of the manipulators. And the condition of maximum contraction—29 mm—is referred as "Ideal Condition".

Also, the experiment of two NiTi SMA springs when connected in series showed that the maximum contraction practically possible is approximately 40 mm at 1200 mA of current supply. Hence, it is necessary to identify the workspace based on the feasible condition that the SMA springs can shrink up to ~40 mm. This condition of 40 mm as the maximum contraction is referred to as "Feasible Condition", and the workspace so obtained is termed as "Feasible Workspace".

The CAD model analysis is repeated again for the family of manipulators discussed here. Two sets of ideal and feasible workspace analyses have been conducted for each manipulator, and the pose of the end-effector was obtained. Table 6 shows the positions of the end-effector of the C1 manipulator under varied conditions of SMA spring actuation. Similar sets of data were obtained for the rest of the manipulators as well. Based on the obtained data, the total stroke length for the end-effector is calculated and is tabulated in Table 7. (Q_x, Q_y) in Table 6 represents the position of the end-effector in the Cartesian coordinate system.

6.2 Comparison study between ideal and feasible workspace

The workspace area associated with the family of manipulators is consolidated in Table 8 based on the data from Table 7. Table 8 indicates the consolidated displacements of the end-effector along both the axes. This table also indicates the loss in the workspace and the loss in

Table 6 End-effector position of C1 manipulator under ideal and feasible conditions

SMA Actuators (conditions)	Direction of spring actuation	Position of the end-effector (mm)							
		Ideal condition				Feasible condition			
		Set 1		Set 2		Set 1		Set 2	
		Q _x	Q _y	Q _x	Q _y	Q _x	Q _y	Q _x	Q _y
r ₁	Initial position	75.500	105.500	125.500	95.500	120.500	100.500	115.500	95.500
	r ₁ :F	135.750	105.500	155.750	95.500	147.000	100.500	132.000	95.500
	r ₁ :B	58.250	105.500	78.250	95.500	97.000	100.500	82.000	95.500
r ₂	Initial position	58.250	105.500	78.250	95.500	97.000	100.500	82.000	95.500
	r ₂ :F	78.380	125.630	88.250	105.500	100.250	103.750	95.250	108.750
	r ₂ :B	44.480	91.730	88.250	105.500	75.250	78.750	70.250	83.750
r ₃	Initial position	44.480	91.730	88.250	105.500	75.250	78.750	70.250	83.750
	r ₃ :F	44.480	91.730	58.120	135.620	53.240	100.760	53.240	100.760
	r ₃ :B	68.110	68.110	88.250	105.500	77.000	77.000	77.000	77.000
r ₁ and r ₂	Initial position	68.110	68.110	88.250	105.500	77.000	77.000	77.000	77.000
	r ₁ :F, r ₂ :B	140.750	63.250	132.120	71.880	127.000	77.000	125.000	77.000
	r ₁ :B, r ₂ :F	88.250	88.250	88.250	105.500	102.000	102.000	102.000	102.000
r ₁ and r ₃	Initial position	88.250	88.250	88.250	105.500	102.000	102.000	102.000	102.000
	r ₁ :F, r ₃ :F	120.360	120.360	135.620	135.620	113.330	113.330	125.000	125.000
	r ₁ :B, r ₃ :B	81.610	81.610	88.250	105.500	88.330	88.330	102.000	100.000
r ₂ and r ₃	Initial position	81.610	81.610	88.250	105.500	88.330	88.330	97.270	104.730
	r ₂ :B, r ₃ :F	44.480	82.020	88.250	105.500	53.240	100.760	53.240	101.240
	r ₂ :B, r ₃ :B	63.250	63.250	63.250	63.250	77.000	77.000	77.000	77.000
r ₁ , r ₂ and r ₃	Initial position	63.250	63.250	63.250	63.250	77.000	77.000	77.000	77.000
	r ₁ :F, r ₂ :B, r ₃ :F	115.750	88.250	115.750	88.250	102.000	102.000	100.000	102.000
	r ₁ :B, r ₂ :F, r ₃ :B	88.250	88.250	88.250	88.250	102.000	102.000	102.000	102.000
	r ₁ :F, r ₂ :F, r ₃ :F	140.750	140.750	140.750	140.750	127.000	127.000	125.000	125.000
	r ₁ :B, r ₂ :F, r ₃ :F	63.250	140.750	63.250	140.750	77.000	127.000	77.000	125.000
	r ₁ :B, r ₂ :B, r ₃ :B	63.250	63.250	63.250	63.250	77.000	77.000	77.000	77.000
	r ₁ :F, r ₂ :B, r ₃ :B	140.750	63.250	140.750	63.250	127.000	77.000	125.000	77.000

‘F’ and ‘B’ represent forward and backward actuation, respectively, at the legs of the manipulator

individual displacements along both the axes. The loss resulted is due to the difference in contraction length between the ideal and feasible conditions.

Table 8 clearly indicates that the total workspace area is highest for C5 under both ideal and feasible conditions. The manipulators C16 and C17 have minimum ideal and feasible workspace areas, respectively. Similarly, it can be identified that under feasible condition, the manipulators C13 and C5 have the maximum displacements along X- and Y-axes, respectively. Although C5 has the highest ideal and feasible workspace area, it has the least percentage loss in the workspace area.

Figure 10 clearly illustrates that the ideal workspace area is more as compared to the feasible workspace area. It also clearly illustrates the variation in the workspace area of all the manipulators.

Figure 11 depicts the loss incurred in each manipulator due to the difference in maximum contraction length between the ideal and the feasible condition. The loss incurred is due to the displacements along individual axes, which in turn leads to a reduction in the workspace area of the manipulators. This plot can be used to identify the performance of the manipulators based on the overall loss incurred.

6.3 Comparison study of end-effector rotation under ideal and feasible conditions

The maximum angular rotation (θ) of the end-effector for each of the eighteen unique manipulators was obtained based on the ideal and feasible condition, as mentioned earlier. Table 9 gives the maximum angular rotation data of

Table 7 Ideal and feasible workspace of all the 18 configured 3-DOF U-shaped base PPMs

Sl. No.	Manipulators	Parameter	Ideal workspace			Feasible workspace		
			Minimum	Maximum	Stroke length	Minimum	Maximum	Stroke length
1	C1	Q _x (mm)	44.48	155.75	111.27	53.24	147.00	93.76
		Q _y (mm)	63.25	140.75	77.50	77.00	127.00	50.00
2	C2	Q _x (mm)	53.07	140.75	87.68	69.47	127.77	58.30
		Q _y (mm)	63.25	140.75	77.50	77.00	127.00	50.00
3	C3	Q _x (mm)	94.00	159.52	65.52	95.13	148.70	53.57
		Q _y (mm)	38.59	159.52	120.93	58.80	114.23	55.43
4	C4	Q _x (mm)	54.37	140.75	86.38	69.16	129.84	60.68
		Q _y (mm)	63.25	140.75	77.50	75.00	124.00	49.00
5	C5	Q _x (mm)	70.64	144.67	74.03	70.51	139.33	68.82
		Q _y (mm)	28.70	167.53	138.83	31.55	166.72	135.17
6	C6	Q _x (mm)	96.19	110.00	13.81	96.39	108.84	12.45
		Q _y (mm)	63.49	158.61	95.12	66.71	146.84	80.13
7	C7	Q _x (mm)	54.37	140.75	86.38	71.05	130.64	59.59
		Q _y (mm)	63.25	140.75	77.50	77.00	127.00	50.00
8	C8	Q _x (mm)	42.73	153.25	110.52	53.04	150.91	97.87
		Q _y (mm)	63.25	140.75	77.50	77.00	127.00	50.00
9	C9	Q _x (mm)	94.00	166.31	72.31	94.24	158.07	63.83
		Q _y (mm)	40.45	147.95	107.50	56.55	132.78	76.23
10	C10	Q _x (mm)	42.22	157.05	114.83	53.88	145.40	91.52
		Q _y (mm)	63.25	140.75	77.50	75.00	124.00	49.00
11	C11	Q _x (mm)	94.01	156.04	62.03	94.06	120.92	26.86
		Q _y (mm)	29.16	163.98	134.82	46.50	146.41	99.91
12	C12	Q _x (mm)	94.48	110.00	15.52	95.18	108.82	13.64
		Q _y (mm)	50.76	164.65	113.89	51.76	94.20	42.44
13	C13	Q _x (mm)	36.00	168.00	132.00	36.00	168.00	132.00
		Q _y (mm)	63.25	110.00	46.75	77.00	110.00	33.00
14	C14	Q _x (mm)	44.44	108.47	64.03	60.10	105.52	45.42
		Q _y (mm)	60.88	109.76	48.88	69.03	106.65	37.62
15	C15	Q _x (mm)	36.00	168.00	132.00	36.33	168.00	131.67
		Q _y (mm)	63.25	110.00	46.75	77.00	109.82	32.82
16	C16	Q _x (mm)	94.14	110.00	15.86	98.16	105.84	7.68
		Q _y (mm)	84.96	109.79	24.83	91.15	109.78	18.63
17	C17	Q _x (mm)	90.64	110.00	19.36	100.29	109.31	9.02
		Q _y (mm)	86.74	109.98	23.24	100.66	109.96	9.30
18	C18	Q _x (mm)	36.22	168.00	131.78	36.51	167.97	131.46
		Q _y (mm)	63.25	109.87	46.62	77.00	109.81	32.81

the end-effector for each of the manipulators. The angular values so mentioned have been obtained by CAD analysis in solid modelling software.

6.4 Experimental workspace analysis

Table 8 and Fig. 10 clearly indicate that the top three manipulators based on maximum feasible workspace area are C5, C8 and C9. Hence, these three manipulators have been considered for further analysis of workspace experimentally by incorporating NiTi SMA springs.

The linear actuation of the manipulators' legs results in a change in position of the end-effector for all the three different selected manipulators. Due to coupled kinematic relations, the end-effector pose varies in the XY plane. The joint of two springs at each leg plays an important role in coordinating linear actuation to the end-effector.

Experiments were conducted in the in-house fabricated prototypes of the three selected manipulators and the end-effector pose was obtained, as depicted in Figs. 12, 13 and 14 based on various combinations of input

Table 8 Consolidated ideal and feasible workspace

Sl. No.	Manipulators	Ideal workspace			Feasible workspace			Percentage loss in workspace (Ideal vs Feasible)		
		X-axis displacement (mm)	Y-axis displacement (mm)	Total workspace (mm ²)	X-axis displacement (mm)	Y-axis displacement (mm)	Total workspace (mm ²)	Reduction along X-axis	Reduction along Y-axis	Total workspace reduction
1	C1	111.27	77.50	8623.43	93.76	50.00	4688.00	15.74	35.48	45.64
2	C2	87.68	77.50	6795.20	58.30	50.00	2915.00	33.51	35.48	57.10
3	C3	65.52	120.93	7923.33	53.57	55.43	2969.39	18.24	54.16	62.52
4	C4	86.38	77.50	6694.45	60.68	49.00	2973.32	29.75	36.77	55.59
5	C5	74.03	138.83	10,277.58	68.82	135.17	9302.40	7.04	2.64	9.49
6	C6	13.81	95.12	1313.61	12.45	80.13	997.62	9.85	15.76	24.06
7	C7	86.38	77.50	6694.45	59.59	50.00	2979.50	31.01	35.48	55.49
8	C8	110.52	77.50	8565.30	97.87	50.00	4893.50	11.45	35.48	42.87
9	C9	72.31	107.50	7773.33	63.83	76.23	4865.76	11.73	29.09	37.40
10	C10	114.83	77.50	8899.33	91.52	49.00	4484.48	20.30	36.77	49.61
11	C11	62.03	134.82	8362.88	26.86	99.91	2683.58	56.70	25.89	67.91
12	C12	15.52	113.89	1767.57	13.64	42.44	578.88	12.11	62.74	67.25
13	C13	132.00	46.75	6171.00	132.00	33.00	4356.00	0.00	29.41	29.41
14	C14	64.03	48.88	3129.79	45.42	37.62	1708.70	29.06	23.04	45.41
15	C15	132.00	46.75	6171.00	131.67	32.82	4321.41	0.25	29.80	29.97
16	C16	15.86	24.83	393.80	7.68	18.63	143.08	51.58	24.97	63.67
17	C17	19.36	23.24	449.93	9.02	9.30	83.89	53.41	59.98	81.36
18	C18	131.78	46.62	6143.58	131.46	32.81	4313.20	0.24	29.62	29.79
Minimum value		13.81	23.24	393.80	7.68	9.30	83.89	0.00	2.64	9.49
Maximum value		132.00	138.83	10,277.58	132.00	135.17	9302.40	56.70	62.74	81.36

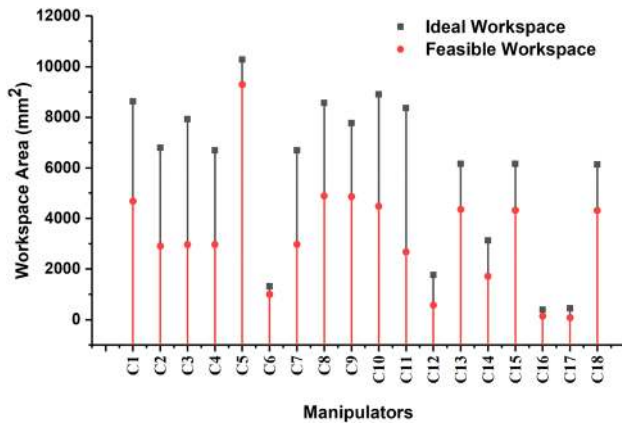


Fig. 10 Ideal and feasible workspace area of manipulators

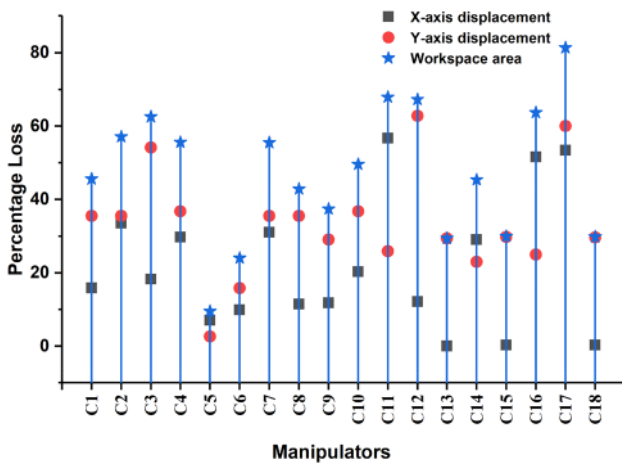


Fig. 11 Percentage loss in workspace

translational units along with the combinations of forward and backward strokes. The experimental data so obtained are presented in Tables 10, 11 and 12.

6.5 Comparison study between feasible and experimental workspace of U-shaped base planar parallel manipulators

The workspace area associated with each of the three experimented manipulators has been compared with the feasible workspace data in Table 13. The table clearly indicates a further decrease in the workspace area under experiment when compared to the feasible workspace area. As interpreted, the workspace area is highest for the C5 manipulator even after a 60.25% loss in the workspace area. The C8 and C5 manipulators provide the highest displacements along X- and Y-axes respectively, within the workspace.

Table 9 Consolidated maximum end-effector rotation under ideal and feasible conditions

Parameter	Condition	Manipulators																		
		C1	C2	C3	C4	C5	C6	C7	C8	C9	C10	C11	C12	C13	C14	C15	C16	C17	C18	
Maximum end-effector angular motion analysis (in degrees)	Ideal	90.06	48.65	116.93	20.80	48.83	46.95	49.42	38.43	65.80	21.00	40.91	38.98	82.97	82.71	18.90	47.03	21.27	20.80	116.93
	Feasible	90.06	30.16	116.93	13.77	43.52	46.95	42.05	37.52	54.87	13.77	35.62	29.12	57.96	58.08	14.88	46.26	13.59	13.77	116.93

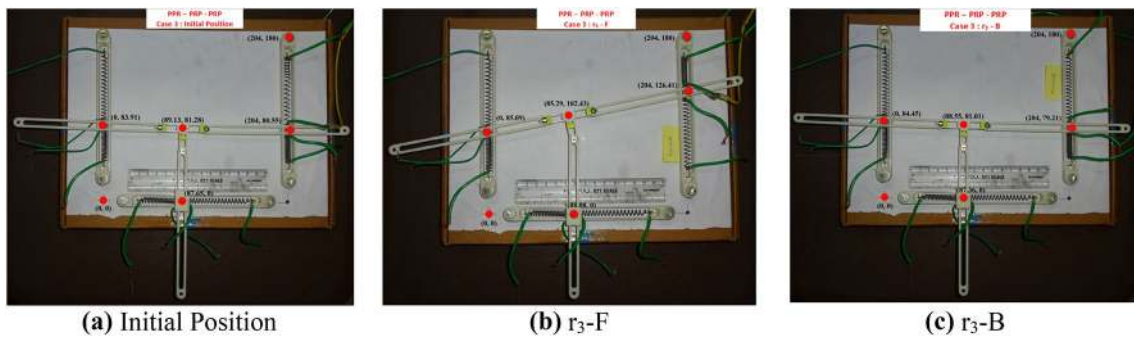


Fig. 12 Actuation of SMA springs of C5 manipulator (Condition 3)

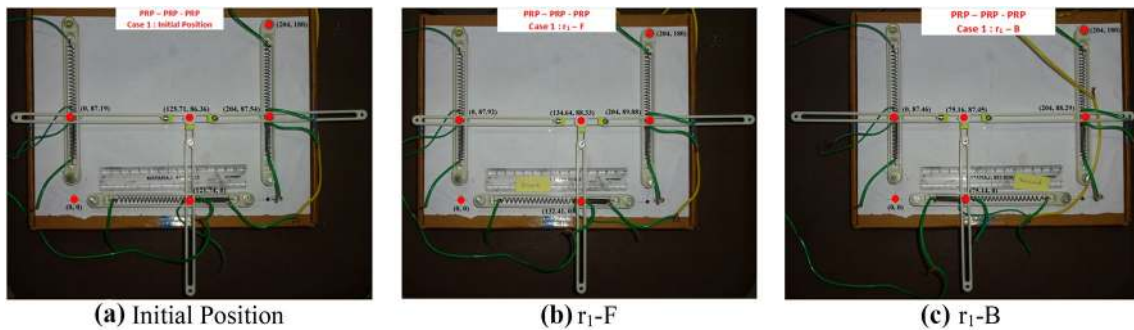


Fig. 13 Actuation of SMA springs of C8 manipulator (Condition 1)

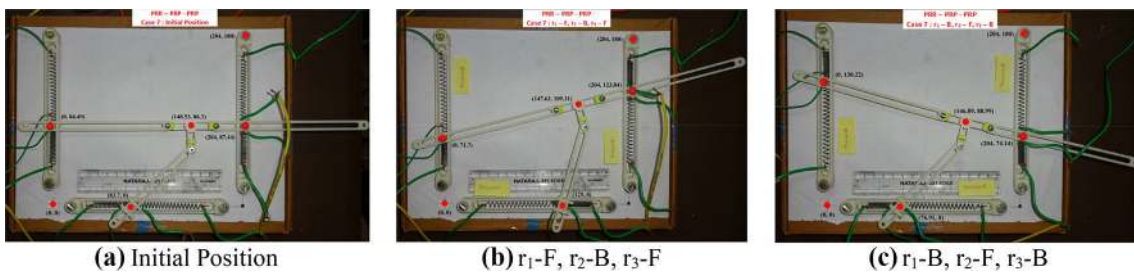


Fig. 14 Actuation of SMA springs of C9 manipulator (Condition 7)

The loss in the experimental workspace area as compared to the feasible workspace area is quantitatively mentioned in Table 13. The loss in the workspace results due to various factors, some of which include—(i) singularities and (ii) friction between mobile parts in contact.

(i) Singularities

Jacobian and the kinematic isotropy are the performance indices of manipulators, as discussed in Sect. 2. Jacobian matrix theoretically dictates the singular positions associated with any manipulator which affects the overall workspace. The kinematic isotropy of various manipulators has already been

presented in the literature [46] which dictates the effect of singularity on the reduction of workspace. Figure 15, resembling the C8 manipulator, depicts the position of the manipulator at which singularity exists. It can be seen that Link 2 is parallel to X-axis and is fully displaced towards the right. Now, even if the actuator r_1 tries to actuate in the forward direction (positive X-axis), the end-effector (represented as a red dot) remains still as it loses its degrees of freedom. The end-effector resists the forces and moments due to the forward actuation of r_1 . Also, at the same position of links and joints, even when r_3 actuates backward (negative Y-axis), the end-effec-

Table 10 Experimental workspace of C5 manipulator

Actuators made of SMA springs (conditions)	Direction of the actuation during heating of the SMA springs	Position of the end-effector							
		Set-1		Set-2		Set-3		Set-4	
		Q _x (mm)	Q _y (mm)	Q _x (mm)	Q _y (mm)	Q _x (mm)	Q _y (mm)	Q _x (mm)	Q _y (mm)
r ₁	Initial position	90.060	102.120	90.700	112.410	92.730	113.150	89.310	108.130
	r ₁ :F (Forward direction)	105.210	139.060	99.210	132.090	108.050	143.510	108.380	144.230
	r ₁ :B (Backward direction)	89.800	108.530	89.570	114.090	88.460	106.880	88.260	107.120
r ₂	Initial position	99.890	136.770	96.250	124.480	96.290	124.880	96.070	125.839
	r ₂ :F (Forward direction)	99.400	144.060	98.250	143.280	99.100	145.909	100.410	143.621
	r ₂ :B (Backward direction)	94.340	122.770	96.450	119.020	95.780	120.900	95.120	120.309
r ₃	Initial position	96.810	124.000	99.550	115.170	98.390	122.319	98.980	118.946
	r ₃ :F (Forward direction)	94.870	128.520	93.620	133.200	93.470	133.618	95.060	132.255
	r ₃ :B (Backward direction)	101.040	112.110	99.980	118.060	100.390	117.614	100.560	113.711
r ₁ and r ₂	Initial position	99.440	118.650	95.710	120.530	97.100	125.441	94.540	119.393
	r ₁ :F and r ₂ :B	109.170	131.690	108.270	133.880	112.780	136.706	108.550	135.833
	r ₁ :B and r ₂ :F	94.340	127.170	95.570	128.550	94.490	121.194	90.830	115.122
r ₁ and r ₃	Initial position	92.090	116.500	90.960	105.730	91.360	108.322	91.320	111.812
	r ₁ :F and r ₃ :F	107.870	157.400	102.640	154.850	105.610	157.740	105.620	156.501
	r ₁ :B and r ₃ :B	88.380	101.050	88.740	98.360	89.100	97.615	87.740	107.600
r ₂ and r ₃	Initial position	89.940	118.050	91.830	87.310	91.700	86.124	91.710	86.129
	r ₂ :B and r ₃ :F	93.630	88.370	92.920	90.070	92.450	86.547	92.240	86.310
	r ₂ :B and r ₃ :B	92.300	83.240	92.220	86.990	91.970	85.538	92.180	85.190
r ₁ , r ₂ and r ₃	Initial position	91.610	86.760	106.590	128.900	104.300	128.368	105.200	128.500
	r ₁ :F, r ₂ :B and r ₃ :F	123.910	59.040	104.850	144.600	104.280	143.753	105.600	144.240
	r ₁ :B, r ₂ :F and r ₃ :B	93.550	77.930	90.190	107.080	89.520	105.609	89.820	106.350
	r ₁ :F, r ₂ :F and r ₃ :F	105.820	156.470	107.640	157.190	108.730	158.144	108.240	157.620
	r ₁ :B, r ₂ :F and r ₃ :F	87.890	127.090	88.100	121.500	88.920	123.772	89.140	122.610
	r ₁ :B, r ₂ :B and r ₃ :B	86.600	83.300	91.060	82.820	89.890	81.651	90.410	82.260
	r ₁ :F, r ₂ :B and r ₃ :B	109.960	127.100	106.720	125.200	107.690	123.023	107.260	124.220

tor is unable to change its position. It is because Link 3 is unable to displace any more along the positive X direction. Hence, it represents the presence of singularity. This kind of singularity is known as an inverse kinematic singularity. It reduces the workspace of PPMs to a large extent. Similarly, there exist direct kinematic and combined singularities in various PPMs, which leads to workspace loss.

(ii) Friction between mobile parts in contact.

The fabricated model has various link joints that are in contact with various elements or parts. As the input translational joint actuates, the motion is transferred by the motion of various links and joints connected in between the end-effector and the input translational joints. As there exists relative motion between the links and the joints, the rela-

tive force and the relative velocity decrease. Due to the loss in the relative forces and the relative velocity, there exists a loss in the stroke length of the input translational joints and the end-effector along both X- and Y-axes. This results in a decrease in the overall workspace of the manipulators.

Figures 16, 17 and 18 clearly depicts the different workspace area in the XY plane associated with each of the manipulators.

The plot in Fig. 19 clearly indicates that the C5 manipulator has a wider workspace length along the Y-axis and the C8 manipulator has a wider workspace length along the X-axis. All the three manipulators acquire different regions in the XY plane within the domain of the mobile platform.

Table 11 Experimental workspace of C8 manipulator

Actuators made of SMA springs (conditions)	Direction of the actuation during heating of the SMA springs	Position of the end-effector							
		Set-1		Set-2		Set-3		Set-4	
		Q _x (mm)	Q _y (mm)	Q _x (mm)	Q _y (mm)	Q _x (mm)	Q _y (mm)	Q _x (mm)	Q _y (mm)
r ₁	Initial position	97.300	93.303	76.530	92.926	77.140	91.636	79.360	93.055
	r ₁ :F (Forward direction)	112.890	94.009	114.410	93.525	109.140	93.376	110.750	93.282
	r ₁ :B (Backward direction)	75.890	93.008	76.670	91.122	78.740	92.910	83.780	91.900
r ₂	Initial position	86.030	93.764	82.670	91.338	84.530	91.823	86.750	91.686
	r ₂ :F (Forward direction)	100.270	116.104	103.560	117.210	110.150	114.686	107.820	114.729
	r ₂ :B (Backward direction)	82.410	84.807	84.640	84.427	86.870	88.484	86.790	88.271
r ₃	Initial position	87.400	93.860	98.180	93.289	87.590	94.041	95.600	93.466
	r ₃ :F (Forward direction)	85.460	102.846	85.680	97.529	84.990	96.509	81.520	96.994
	r ₃ :B (Backward direction)	99.350	91.413	87.670	94.428	96.340	93.059	97.580	92.629
r ₁ and r ₂	Initial position	97.440	94.385	107.590	113.468	112.750	111.784	112.810	110.333
	r ₁ :F and r ₂ :B	108.830	85.519	113.600	89.064	113.860	88.755	113.110	87.108
	r ₁ :B and r ₂ :F	107.990	114.134	113.330	113.313	113.450	116.829	112.720	114.918
r ₁ and r ₃	Initial position	107.490	108.712	104.150	109.092	88.690	109.788	96.480	109.845
	r ₁ :F and r ₃ :F	113.620	112.861	121.600	110.534	114.050	111.636	124.360	112.528
	r ₁ :B and r ₃ :B	103.910	106.575	88.690	108.336	96.140	107.757	98.770	108.193
r ₂ and r ₃	Initial position	99.130	109.382	81.220	90.025	78.790	90.953	82.430	90.015
	r ₂ :B and r ₃ :F	76.580	87.847	77.300	86.275	73.440	87.118	74.370	87.810
	r ₂ :B and r ₃ :B	86.820	81.173	79.100	82.077	81.950	81.775	81.100	82.219
r ₁ , r ₂ and r ₃	Initial position	81.240	90.231	107.780	92.710	109.260	93.573	109.110	104.509
	r ₁ :F, r ₂ :B and r ₃ :F	94.510	87.336	102.890	88.848	98.760	92.660	103.390	91.037
	r ₁ :B, r ₂ :F and r ₃ :B	110.340	115.071	111.120	114.891	113.590	112.385	114.390	112.977
	r ₁ :F, r ₂ :F and r ₃ :F	113.550	120.141	115.180	117.695	109.530	117.464	119.210	121.473
	r ₁ :B, r ₂ :F and r ₃ :F	85.160	121.085	107.390	117.248	97.110	116.580	86.080	120.983
	r ₁ :B, r ₂ :B and r ₃ :B	80.000	85.105	87.050	90.305	87.530	91.695	78.610	84.248
	r ₁ :F, r ₂ :B and r ₃ :B	113.880	85.490	109.490	94.561	108.610	91.375	117.910	81.643

6.6 Comparison study of end-effector rotation under ideal, feasible and experimental conditions

The maximum angular rotation (θ) of the end-effector for the selected three manipulators was determined experimentally based on the observations mentioned under Tables 10, 11 and 12. The experimentally obtained maximum angular rotation was compared with the maximum angular rotation obtained under ideal and feasible conditions and mentioned in Table 14 which gives the maximum angular rotation data of the end-effector for each of the manipulators.

7 Conclusion

The major conclusions of this study have been outlined below:

1. The correlation between the active translational joint and the pose of the end-effector for various possible kinematic limb conditions has been derived.
2. The Jacobian matrices for the family of U-shape base 3-DOF planar parallel manipulators have been formulated.
3. The workspace area based on ideal and feasible conditions was predicted for all the eighteen unique PPMs. The manipulator with the maximum ideal and feasible workspace area is $\underline{PPR}\text{-}\underline{PRP}\text{-}\underline{PRR}$ with an area of 10277.58 mm² and 9302.40 mm², respectively. On the other hand, $\underline{PRR}\text{-}\underline{PRR}\text{-}\underline{PRR}$ had a minimum ideal workspace area of 393.80 mm² and $\underline{PRR}\text{-}\underline{PRR}\text{-}\underline{PRP}$ had a minimum feasible workspace area of 83.89 mm².
4. The three manipulators $\underline{PPR}\text{-}\underline{PRP}\text{-}\underline{PRR}$, $\underline{PRP}\text{-}\underline{PPR}\text{-}\underline{PRP}$ and $\underline{PRP}\text{-}\underline{PPR}\text{-}\underline{PRR}$ with higher workspace area of 9302.40 mm², 4893.50 mm² and 4865.76 mm² were further experimented.

Table 12 Experimental workspace of C9 manipulator

Actuators made of SMA springs (conditions)	Direction of the actuation during heating of the SMA springs	Position of the end-effector							
		Set-1		Set-2		Set-3		Set-4	
		Q _x (mm)	Q _y (mm)	Q _x (mm)	Q _y (mm)	Q _x (mm)	Q _y (mm)	Q _x (mm)	Q _y (mm)
r ₁	Initial position	99.563	95.713	99.176	93.318	99.237	96.117	99.064	96.580
	r ₁ :F (Forward direction)	99.829	100.152	99.339	100.596	99.329	94.568	99.023	96.769
	r ₁ :B (Backward direction)	99.247	93.324	99.053	96.257	98.890	96.453	99.176	94.851
r ₂	Initial position	98.819	96.959	98.503	91.713	98.645	92.952	98.543	90.578
	r ₂ :F (Forward direction)	100.767	123.887	100.634	124.468	101.063	122.321	100.114	119.876
	r ₂ :B (Backward direction)	98.921	86.692	99.227	86.312	98.788	86.842	99.227	84.156
r ₃	Initial position	98.411	91.585	98.044	93.973	98.217	93.838	98.533	93.392
	r ₃ :F (Forward direction)	100.175	89.819	99.971	91.362	100.022	92.537	100.920	92.271
	r ₃ :B (Backward direction)	98.482	91.807	98.431	92.692	98.645	92.406	98.533	92.108
r ₁ and r ₂	Initial position	98.431	94.112	98.931	115.635	98.798	113.944	98.717	114.580
	r ₁ :F and r ₂ :B	98.900	89.222	98.554	92.765	98.431	94.984	98.390	93.572
	r ₁ :B and r ₂ :F	99.676	121.637	99.594	118.487	99.319	119.234	100.033	123.144
r ₁ and r ₃	Initial position	98.584	116.460	96.534	112.440	97.238	112.847	97.452	111.834
	r ₁ :F and r ₃ :F	96.299	119.428	96.850	118.540	96.116	118.145	96.208	113.106
	r ₁ :B and r ₃ :B	97.544	112.932	97.880	112.109	97.289	111.146	97.768	113.154
r ₂ and r ₃	Initial position	97.075	111.900	95.534	85.312	95.718	89.055	95.861	88.661
	r ₂ :B and r ₃ :F	99.104	88.610	98.737	84.780	98.574	84.890	98.472	84.040
	r ₂ :B and r ₃ :B	96.136	83.217	95.922	82.024	97.156	81.618	96.126	83.933
r ₁ , r ₂ and r ₃	Initial position	96.534	84.262	95.738	92.865	95.626	94.938	95.330	94.528
	r ₁ :F, r ₂ :B and r ₃ :F	97.085	85.501	97.126	88.203	96.493	89.047	96.140	88.235
	r ₁ :B, r ₂ :F and r ₃ :B	97.350	119.089	98.023	118.826	97.013	114.720	95.600	114.625
	r ₁ :F, r ₂ :F and r ₃ :F	96.656	126.479	96.646	125.971	97.095	125.730	96.540	117.983
	r ₁ :B, r ₂ :F and r ₃ :F	95.626	123.710	95.626	120.184	96.034	119.203	95.210	118.276
	r ₁ :B, r ₂ :B and r ₃ :B	96.820	78.853	96.605	82.081	97.146	84.347	96.180	85.563
	r ₁ :F, r ₂ :B and r ₃ :B	96.575	89.317	97.105	86.435	97.258	88.056	99.829	92.447

- The PPR-PRP-PRR manipulator was found to possess the highest experimental workspace area than any other combination.
 - The PPR-PRP-PRR manipulator was also found to possess the highest angular motion of 33° based on the experiment conducted.
 - The developed micro-motion stage can be incorporated wherever X- and Y-axis motion is required with micron-level accuracy.
- The developed manipulator prototype can further be implemented for the process of micro-milling operation,

Table 13 Consolidated feasible and experimental workspace

Sl. No.	Manipulators	Feasible workspace		Experimental workspace		Percentage loss in workspace (feasible vs experimental)		
		X-axis displacement (mm)	Y-axis displacement (mm)	X-axis displacement (mm)	Y-axis displacement (mm)	Reduction along X-axis	Reduction along Y-axis	Total workspace reduction
1	C5	68.82	135.17	37.31	99.10	45.79	26.68	60.25
2	C8	97.87	50.00	50.92	40.30	47.97	19.40	58.07
3	C9	63.83	76.23	5.85	47.63	90.83	37.52	94.27
	Minimum Value	63.83	50.00	5.85	40.30	45.79	19.40	58.07
	Maximum Value	97.87	135.17	50.92	99.10	90.83	37.52	94.27

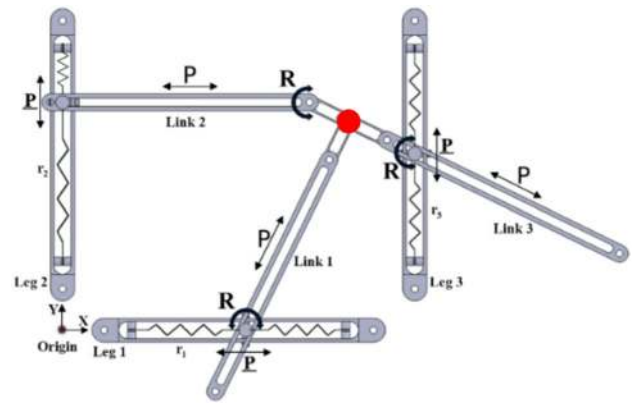


Fig. 15 C8 manipulator

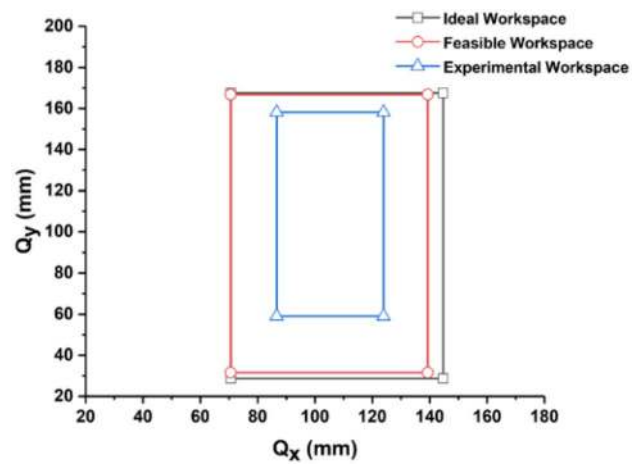


Fig. 16 Workspace area of C5 manipulator

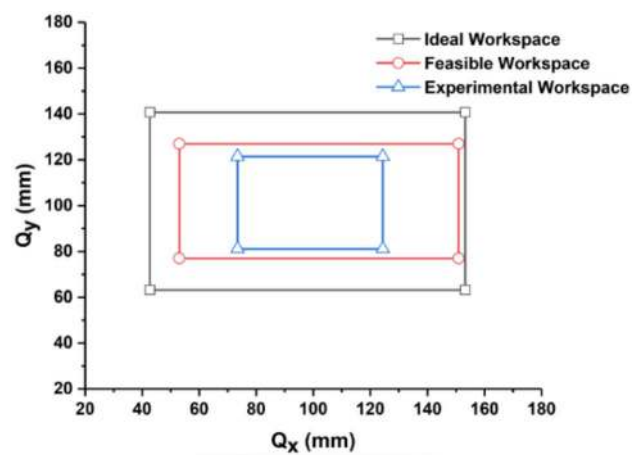


Fig. 17 Workspace area of C8 manipulator

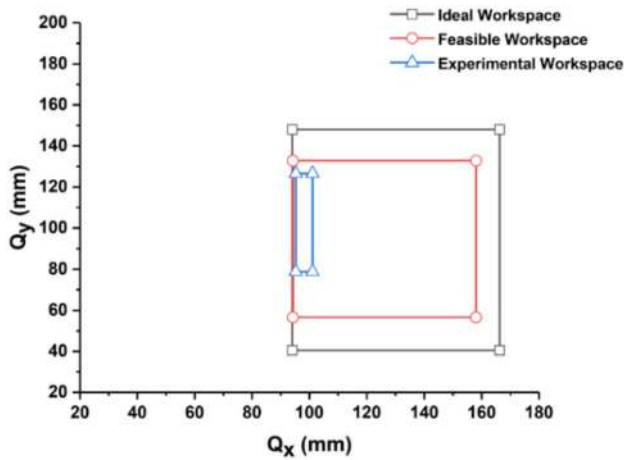


Fig. 18 Workspace Area of C9 Manipulator

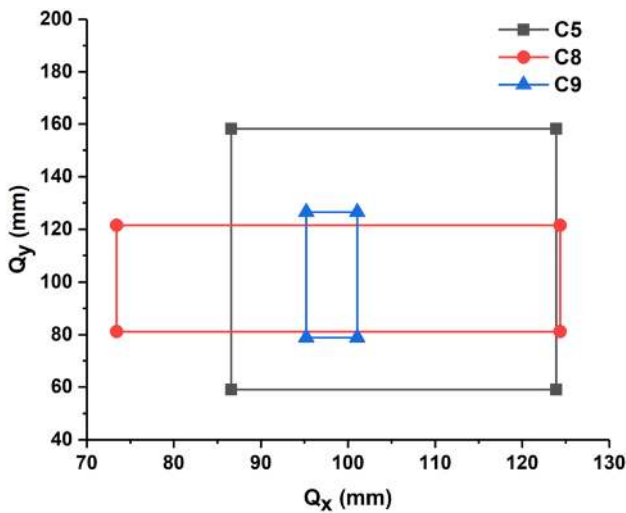


Fig. 19 Experimental workspace area of manipulators

micro-3D printer and other operations too. A three-axis motion stage with SMA spring-based smart actuator can be developed for various three-dimensional applications.

Acknowledgements The presented work in the paper is supported and funded by the CSIR-EMR-II, India (No. 22(0831)/19/EMR-II), and Start-up Research Grant, SERB, DST, India (No. SRG/2020/000491).

Declarations

Conflict of interest On behalf of all authors, the corresponding author states that there is no conflict of interest.

Open Access This article is licensed under a Creative Commons Attribution 4.0 International License, which permits use, sharing, adaptation, distribution and reproduction in any medium or format, as long as you give appropriate credit to the original author(s) and the source, provide a link to the Creative Commons licence, and indicate if changes were made. The images or other third party material in this article are included in the article's Creative Commons licence, unless indicated otherwise in a credit line to the material. If material is not included in the article's Creative Commons licence and your intended use is not permitted by statutory regulation or exceeds the permitted use, you will need to obtain permission directly from the copyright holder. To view a copy of this licence, visit <http://creativecommons.org/licenses/by/4.0/>.

References

1. Briot S, Bonev IA (2010) Are parallel robots more accurate than serial robots? *Trans Can Soc Mech Eng* 31:445–455
2. Dasgupta B, Mruthyunjaya TS (2000) The Stewart platform manipulator: a review. *Mech Mach Theory* 35:15–40
3. Merlet JP (2006) *Parallel robots*, 2nd edn. Springer, Netherlands
4. Patel Y, George P (2012) Parallel manipulators applications—a survey. *Mod Mech Eng* 2(3):57–64
5. Singh D, Singh Y (2018) Development and analysis of a five degrees of freedom robotic manipulator serving as a goal-keeper to train the football players. *IOP Conf Ser Mater Sci Eng* 402(1):012092
6. Staicu S (2009) Inverse dynamics of the 3-PRR planar parallel robot. *Robot Auton Syst* 57(5):556–563
7. Joubair A, Slamani M, Bonev IA (2012) A novel XY-Theta precision table and a geometric procedure for its kinematic calibration. *Robot Comput Integr Manuf* 28:57–65
8. Staicu S (2009) Inverse dynamics of the 3-PRR planar parallel robot. *Robot Auton Syst* 57:556–563

Table 14 Consolidated maximum end-effector rotation under ideal, feasible and experimental conditions

Sl. No.	Manipulators	Maximum end-effector angular motion analysis (in degrees)		
		Ideal condition	Feasible condition	Experimental condition
1	C5	48.83	43.52	33.00
2	C8	38.43	37.52	16.00
3	C9	65.80	54.87	27.00
Minimum value		38.43	37.52	16.00
Maximum value		65.80	54.87	33.00

9. Choi KB (2003) Kinematic analysis and optimal design of 3-PPR planar parallel manipulator. *KSME Int J* 17:528–537
10. Bai S, Caro S (2009) Design and analysis of a 3-PPR planar robot with U-shape base. In: ICAR International conference on advanced robotics, pp 1–6
11. Bonev IA (2010) Planar parallel mechanism and method. US Patent 7707907B2
12. Wu J, Wang J, Wang L, You Z (2010) Performance comparison of three planar 3 dof parallel manipulators with 4-RRR, 3-RRR and 2-RRR structures. *Mechatronics* 20(4):510–517
13. Rezaei A, Akbarzadeh A (2013) Position and stiffness analysis of a new asymmetric 2PRR-PPR parallel CNC machine. *Adv Robot* 27(2):133–145
14. Gogu G (2008) Structural synthesis of parallel robots. Part 1: methodology, 1st edn. Springer, Netherlands
15. Gogu G (2009) Structural synthesis of parallel robots. Part 2: translational topologies with two and three degrees of freedom, 1st edn. Springer, Netherlands
16. Gogu G (2010) Structural synthesis of parallel robots. Part 3: topologies with planar motion of the moving platform, 1st edn. Springer, Netherlands
17. Khan WA, Krovi VN, Saha SK, Angeles J (2005) Recursive kinematics and inverse dynamics for a planar 3R parallel manipulator. *J Dyn Syst Meas Control* 127:529–536
18. Wenger P, Chablat D, Zein M (2007) Degeneracy study of the forward kinematics of planar 3-RPR parallel manipulators. *J Mech Des* 129:1265–1268
19. Yu A, Bonev IA, Murray PZ (2008) Geometric approach to the accuracy analysis of a class of 3-dof planar parallel robots. *Mech Mach Theory* 43:364–375
20. Arakelian VH, Smith MR (2008) Design of planar 3-dof 3-RRR reactionless parallel manipulators. *Mechatronics* 18:601–606
21. Briot S, Bonev IA (2008) Accuracy analysis of 3-dof planar parallel robots. *Mech Mach Theory* 43:445–458
22. Staicu S (2008) Dynamics of a 3-RPR planar parallel robot. *UPB Sci Bull Series D* 70(3)
23. Yu A, Bonev IA, Zsombor-Murray P (2006) New XY-Theta positioning table with partially decoupled parallel kinematics. In: Proceedings of the IEEE international symposium on industrial electronics, pp 3108–3112
24. Caro S, Binaud N, Wenger P (2009) Sensitivity analysis of 3-RPR planar parallel manipulators. *J Mech Des* 131(12):121005
25. Wu J, Wang J, You Z (2011) A comparison study on the dynamics of planar 3-dof 4-RRR, 3-RRR and 2-RRR parallel manipulators. *Robot Comput Integr Manuf* 27(1):150–156
26. Wu G, Bai S, Kepler JA, Caro S (2012) Error modelling and experimental validation of a planar 3-PPR parallel manipulator with joint clearance. *J Mech Robot* 4(4):041008
27. Wu J, Li T, Wang J, Wang L (2013) Performance analysis and comparison of planar 3-dof parallel manipulators with one and two additional branches. *J Intell Rob Syst* 72:73–82
28. Caro S, Chablat D, Ur-Rehman R, Wenger P (2011) Multi-objective design optimization of 3-PRR planar parallel manipulators. In: 20th CIRP Design conference. (pp. 373–383)
29. Williams RL, Joshi AR (1999) Planar parallel 3-RPR manipulator. In: conference on applied mechanisms and robotics
30. Yang Y, Brien JF (2007) A case study of the planar 3-RPR parallel robot singularity free workspace design. In: Proceedings of IEEE international conference on mechatronics and automation. (pp. 1834–1838)
31. Staicu S (2009) Power requirement comparison in the 3-RPR planar parallel robot dynamics. *Mech Mach Theory* 44:1045–1057
32. Vinoth V, Singh Y, Mohan S (2014) Indirect disturbance compensation control of a planar parallel (2-PRP and 1-PPR) robotic manipulator. *Robot Comput Int Manuf* 30(5):556–564
33. Singh Y, Mohan S (2015) Inverse dynamics and robust sliding mode control of a planar parallel (2-PRP and 1-PPR) robot augmented with a nonlinear disturbance observer. *Mech Mach Theory* 92:29–50
34. Londhe PS, Singh Y, Mohan S, Patre B, Waghmare LM (2016) Robust nonlinear PID-like fuzzy logic control of a planar parallel (2PRP-PPR) manipulator. *ISA Trans* 63:218–232
35. Singh Y, Vinoth V, Kiran YR, Mohanta JK, Mohan S (2015) Inverse dynamics and control of a 3-DOF planar parallel robotic (U-Shaped 3-PPR) manipulator. *Robot Comput Int Manuf* 34:164–179
36. Singh Y (2016) Performance investigations on mechanical design and motion control of planar parallel manipulators. Ph.D. Thesis, Indian Institute of Technology Indore.
37. Wu J, Wang J, Wang L, Li T (2009) Dynamics and control of a planar 3-DOF parallel manipulator with actuation redundancy. *Mech Mach Theory* 44:835–849
38. Wu J, Wang D, Wang L (2015) A control strategy of a two degrees-of-freedom heavy duty parallel manipulator. *J Dyn Syst Meas Control* 137(6):061007
39. Wu J, Gao Y, Zhang B, Wang L (2017) Workspace and dynamic performance evaluation of the parallel manipulators in a spray-painting equipment. *Robot Comput Int Manuf* 44:199–207
40. Merlet JP (1996) Direct kinematics of planar parallel manipulators. In: robotics and automation. In: Proceedings 1996 IEEE international conference on robotics and automation, pp 3744–3749
41. Chablat D, Wenger P (2007) The kinematic analysis of a symmetrical three-degree-of-freedom planar parallel manipulator. *CoRR*
42. Merlet JP, Gosselin CM, Mouly N (1998) Workspaces of planar parallel manipulators. *Mech Mach Theory* 33(1–2):7–20
43. Wu G, Bai S, Kepler J (2015) Stiffness characterization of a 3-PPR planar parallel manipulator with actuation compliance. *Proc Ins Mech Eng Part C J Mech Eng Sci* 229(12):2291–2302
44. Bai S, Caro S (2009) Design and analysis of a 3-PPR planar robot with U-shape base. In: 2009 International conference on advanced robotics
45. Gosselin CM, Angeles J (1988) The optimum kinematic design of a planar three-degree-of-freedom parallel manipulator. *J Mech Transm Autom Design* 110(1):35–41
46. Mohanta J, Singh Y, Mohan S (2018) Kinematic and dynamic performance investigations of asymmetric (U-shape fixed base) planar parallel manipulators. *Robotica* 36(8):1111–1143
47. AbuZaiter A, Ng EL, Kazi S, Ali MSM (2015) Development of miniature stewart platform using TiNiCu shape-memory-alloy actuators. *Adv Mater Sci Eng* 928139
48. AbuZaiter A, Hikmat OF, Nafea M, Ali MSM (2016) Design and fabrication of a novel XY θ z monolithic micro-positioning stage driven by NiTi shape-memory-alloy actuators. *Smart Mater Struct* 25(10):105004
49. Sreekumar M, Singaperumal M, Nagarajan T, Zoppi M, Molfino R (2006) A compliant miniature parallel manipulator with shape memory alloy actuators. In: 2006 IEEE International conference on industrial technology, Mumbai. (pp. 848–853)
50. Singh Y, Mohan S (2017) Development of a planar 3PRP planar parallel manipulator using shape memory alloy spring based actuators. In: Proceedings of the advances in robotics (Proceeding AIR'17). pp 1–6
51. Singh D, Choudhury R, Singh Y, Mukherjee M (2020) Development and workspace analysis of smart actuation based planar parallel robotic motion stage. *IOP Conf Ser Mater Sci Eng* 912:032063
52. Paik JK, Wood RJ (2012) A bidirectional shape memory alloy folding actuator. *Smart Mater Struct* 21(6):065013

53. Singh D, Singh Y, Mukherjee M (2021) Behaviour of NiTi based smart actuator for the development of planar parallel micro-motion stage. In: Kalamkar V, Monokova K (eds) *Advances in mechanical engineering. Lecture notes in mechanical engineering*. Springer, Singapore, pp 221–228
54. Miková L, Medvecká-Beňová S, Kelemen M, Trebuňa F, Virgala I (2015) Application of shape memory alloy (SMA) as actuator. *METABK* 54(1):169–172
55. Leng J, Yan X, Zhang X, Huang D, Gao Z (2016) Design of a novel flexible shape memory alloy actuator with multilayer tubular structure for easy integration into a confined space. *Smart Mater Struct* 25(2):025007
56. Huang W (2002) On the selection of shape memory alloys for actuators. *Mater Des* 23(1):11–19
57. Sun L, Huang WM, Ding Z, Zhao Y, Wang CC, Purnawali H, Tang C (2012) Stimulus-responsive shape memory materials: a review. *Mater Des* 33:577–640
58. DesRoches R, McCormick J, Delemont M (2004) Cyclical properties of superelastic shape memory alloy wires and bars. *ASCE J Struct Eng* 130(1):38–46
59. Khidir EA, Mohamed NA, Nor MJM, Mustafa MM (2008) A new method for actuating parallel manipulators. *Sens Actuators A Phys* 147(2):593–599
60. Angeles J (2014) *Fundamentals of robotic mechanical systems: Theory, methods, and algorithms*, 4th edn. Springer, NY, USA

Publisher's Note Springer Nature remains neutral with regard to jurisdictional claims in published maps and institutional affiliations.